Enhancing Fracture Network Characterization: A Data-Driven, Outcrop-Based Analysis

Weiwei Zhu[1], Xupeng He[2], Ryan, Santoso[3], Gang Lei[4], Tad Patzek[2], Moran Wang[1]

[1]Tsinghua University, Beijing, China.
[2]King Abdullah University of Science and Technology, Thuwal, KSA.
[3]RWTH Aachen University, Aachen, Germany
[4]China University of Geosciences, Wuhan, China

Key Points:

- An accurate, robust and efficient pixel-based algorithm is proposed to detect fractures from binary outcrop maps.
- Different fracture properties are systematically investigated with 80 published outcrop maps.
- Justifications and improvements to current discrete fracture networks are summarized.

Corresponding author: Moran Wang, mrwang@tsinghua.edu.cn

Abstract

The stochastic discrete fracture network (SDFN) model is a practical approach to model complex fracture systems in the subsurface. However, it is impossible to validate the correctness and quality of an SDFN model because the comprehensive subsurface structure is never known. We utilize a pixel-based fracture detection algorithm to digitize 80 published outcrop maps of different scales at different locations. The key fracture properties, including fracture lengths, orientations, intensities, topological structures, clusters and flow are then analyzed. Our findings provide significant justifications for statistical distributions used in SDFN modellings. In addition, the shortcomings of current SDFN models are discussed. We find that fracture lengths follow multiple (instead of single) power-law distributions with varying exponents. Large fractures tend to have large exponents, possibly because of a small coalescence probability. Most small-scale natural fracture networks have scattered orientations, corresponding to a small κ value ($\kappa < 3$) in a von Mises–Fisher distribution. Large fracture systems collected in this research usually have more concentrated orientations with large κ values. Fracture intensities are spatially clustered at all scales. A fractal spatial density distribution, which introduces clustered fracture positions, can better capture the spatial clustering than a uniform distribution. Natural fracture networks usually have a significant proportion of T-type nodes, which is unavailable in conventional SDFN models. Thus a rule-based algorithm to mimic the fracture growth and form T-type nodes is necessary. Most outcrop maps show good topological connectivity. However, sealing patterns and stress impact must be considered to evaluate the hydraulic connectivity of fracture networks.

1 Introduction

Fractures, a general concept of discontinuities in geology, includes joints, faults, pressure solution seams and deformation bands. They are ubiquitous in crust rocks and usually comprise complex networks. Fracture networks control many physical properties of rocks, such as stiffness, strength, permeability [*Adler and Thovert*, 1999]. Therefore, they have a significant impact on many engineering fields, such as hydrology, waste disposal, geothermal exploitation, mining, and petroleum reservoir exploitation [*Berkowitz*, 2002; *Dverstorp et al.*, 1992; *Hyman et al.*, 2015; *Dong et al.*, 2019; *He et al.*, 2021].

However, the three-dimensional, small-scale structures of subsurface fractures are largely inaccessible with current technologies (seismic surveys, well logging, field observations, etc.). Furthermore, complex and irregular fracture shapes [*Gertsch*, 1995], rough fracture surfaces [*Zimmerman et al.*, 1991], turtuosity of flow paths in a fracture and stress impact on the

fracture permeability [*Cook et al.*, 1990; *Tsang*, 1984] make it extremely difficult to characterize fracture networks in great detail. A stochastic discrete fracture network model (SDFN) [*Robinson*, 1983; *Andresen et al.*, 2013; *Wilcock*, 1996; *Zhu et al.*, 2019] is possibly the only practical approach to model complex fracture systems in the subsurface. In a stochastic discrete fracture network model, fractures are represented explicitly with simple geometries, such as line segments in 2D and polygons or ellipses in 3D.

Different distributions are implemented to characterize the key geometric properties of the fracture network, including fracture lengths, orientations, and positions of fracture centers. Different researchers propose exponential, gamma, log-normal and power-law distributions to describe fracture lengths [*Priest and Hudson*, 1976; *Davy*, 1993; *Rouleau and Gale*, 1985; *Sornette and Sornette*, 1999]. Field observations and analogue experiments suggest the prevalence of power-law distribution [*Segall and Pollard*, 1983a; *Sornette et al.*, 1993]. The orientation of fractures is usually described by a von Mises–Fisher distribution [*Song et al.*, 2001; *Whitaker and Engelder*, 2005]. Uniform and fractal spatial density distribution are commonly applied to describe positions of fracture centers [*Bour and Davy*, 1997; *Darcel et al.*, 2003]. A fractal dimension characterizes a fractal spatial density distribution. In 2D, the fractal spatial density distribution generates clustered fracture positions and brings clustering effects when the fractal dimension is smaller than 2. It reduces to a uniform distribution when the fractal dimension equals 2. Similarly, in 3D, the corresponding limiting dimension for uniform fracture distribution is 3. A uniform spatial density distribution is easy for implementation but usually unrealistic. Through outcrop observations, natural fracture systems usually show clustering effects [*Bonnet et al.*, 2001; *Zhu et al.*, 2018]. Table. 1 summarizes key geometric properties of fracture networks and their commonly adopted statistical distributions.

A stochastic discrete fracture network cannot characterize details of fracture geometry, but it can preserve the essential topological structure of a fracture network, which determines the overall hydraulic diffusivity in fluid flow through low permeability formations [*Zhu et al.*, 2021a]. Important flow results, such as flow rate or flow-based permeability, are sensitive to fracture configurations. Therefore, it is necessary to investigate fracture configurations before incorporating impacts of detailed fracture properties, such as roughness, curved shapes, and stress impacts. However, actual subsurface fracture networks are unavailable with current technologies. Therefore, it is impossible to validate the correctness and quality of SDFN models. The confidence of SDFN models depends on whether statistical distributions are representative of real fracture networks. Those statistical distributions are usually summarized from available datasets, including outcrop maps[*Ukar et al.*, 2019; *Bisdom et al.*, 2014], wellbore images[*Williams and Johnson*, 2004], and seismic maps [*Prioul*

Table 1. Distributions of different fracture geometric properties

Property	Distribution	Reference
Length	Exponential	*Priest and Hudson* [1976]; *Nur* [1982]
	Gamma	*Davy* [1993]; *Sornette and Sornette* [1999]
	Lognormal	*Priest and Hudson* [1981]; *Rouleau and Gale* [1985]
	Power-law	*Segall and Pollard* [1983a]; *Sornette et al.* [1993]
Orientation	von Mises–Fisher distribution	*Song et al.* [2001]; *Kemeny and Post* [2003]
Position	Uniform	*Berkowitz* [1995]; *Bour and Davy* [1997]
	Fractal	*Darcel et al.* [2003]; *Zhu et al.* [2018]

and Jocker, 2009]. Outcrop maps are essential datasets because they are widely spread and provide abundant information on geometric properties of fractures, such as fracture lengths, orientations, and intersection relationships. However, outcrop maps require a significant human effort to recognize and detect fractures before summarizing statistics. Geologists usually analyze a few outcrop maps at a given region and hardly extend their findings to more general conditions, considering the tremendous time cost for fracture interpretations. Therefore, a synthetic analysis of fracture geometries with a large number of outcrop maps from different scales and locations is unavailable.

To reduce the human effort of interpreting outcrop maps, we have proposed an automatic fracture interpretation algorithm [*Zhu et al.*, 2020], which automatically interprets typical plan-view maps of fracture networks from a variety of resources, such as seismic reflection horizons, satellite images, aerial photos, etc. The method comprises two stages: (1) conversion of a multi-bit per pixel raw outcrop image to a binary map that preserves fracture geometry and connectivity. This stage is denoted as fracture recognition, which is completed by using a deep-learning architecture, U-net [*Ronneberger et al.*, 2015]. (2) replacement of the binary fracture images with line segments or polylines. This stage is named fracture detection, which is completed with a pixel-based fracture detection algorithm. The algorithm is further optimized in this research and discussed in detail in the following section. The deep-learning-based fracture recognition needs many training images, which are unavailable in this research. Therefore, we focus on the fracture detection algorithm and utilize the algorithm to digitize 80 outcrop maps from published literature.

Commonly used lineament detection methods include Hough transform [*Wang and Howarth*, 1990], Segment Tracing Algorithm [*Koike et al.*, 1995] and more methods are available in a detailed review paper [*Ahmadi and Pekkan*, 2021]. Those lineament detection methods are usually sensitive to curved shapes of real fracture traces, thus not suitable for complex fracture systems. Our proposed pixel-based detection algorithm instead is robust, accurate and efficient. All pixels in a fracture trace is recorded, and key information of the fracture trace is available, including fracture lengths, orientations, positions and the abutment relationship between fractures.

The outcrop maps are collected from different locations with varying scales from millimeters to tens of kilometers. We synthetically analyze distributions of fracture lengths, orientations, intensities, topological structures,clusters and flow from those outcrop maps. The findings on fracture geometries provide significant supports and justifications for SDFN modelling, and we also point out shortcomings and possible improvements of the commonly adopted SDFN techniques. The analysis on clusters and flow investigates the connected fractures and their permeability considering stress impacts.

The structure of the paper is organized as follows: Section 2 introduces detailed algorithms used in detecting fractures from binary outcrop maps. Section 3 analyzes distributions of fracture lengths, orientations, intensities, their topological structures, clusters and flow. Section 4 discusses insights for stochastic discrete fracture network modeling. Important findings and conclusions are summarized in Section 5.

2 Fracture detection

A successful interpretation of fractures from a raw outcrop image requires two stages [*Zhu et al.*, 2020]: fracture recognition and fracture detection. Deep learning technique, such as U-net [*Ronneberger et al.*, 2015; *Santoso et al.*, 2019; *Zhu et al.*, 2020], and mathematic methods, such as shearlet transform [*Reisenhofer*, 2014], are suitable for fracture recognition and separate fracture geometries from complex environments. This research collects published binary outcrop maps recognized by different geologists; therefore, the fracture recognition process is irrelevant. A fracture detection process is required to convert binary outcrop maps to line segments or polylines for further in-depth investigations. In our approach, we use a pixel-based fracture detection method that is robust, accurate and efficient. The method is composed of four main steps.

Step 1 Convert a binary image to its skeleton (1-pixel wide image). A Matlab function, 'bwskel' (skeletonization operations on binary images), can easily convert a binary image to its skeleton. An example is shown in Fig. 2(b). Outcrops have experienced

server weathering and stress-release during the upward movement, which significantly changes fracture apertures. Therefore, the aperture information from an outcrop map is generally unreliable. The skeletonization loses the aperture information but preserves the topological structure of the fracture network, which is essential for the flow behaviour in the subsurface.

Step 2 Find initial pixels and intersection pixels of fractures. In the skeleton image, an initial pixel is defined as a pixel with only one neighbouring pixel, and an intersection pixel is defined as a pixel with at least three neighbouring pixels. The pixel with only two neighbouring pixels is named a transit pixel. Fig. 2(c) shows a sketch map of different types of pixels. The green square points represent initial pixels. The blue circle points represent intersection pixels. The red triangle points represent merged intersection pixels. We merge the blue adjacent intersection pixels to their centroid point (red triangle point).

Step 3 Track the trace of a fracture (Type 1 fracture) constrained by a pair of initial pixels or an initial pixel and a merged intersection pixel. The tracking starts at an unvisited initial pixel and stops at the other initial pixel or an isolated intersection pixel (after which there is no valid subsequent pixel) encountered during the tracking. Record all the pixels in a specific fracture trace. The tracking continues until all initial pixels are visited. The green lines marked in Fig. 2(d) are the results of the tracking.

Step 4 Track the trace of a fracture (Type 2 fracture) constrained by a pair of merged intersection pixels. The tracking starts at a merged intersection pixel and stops at the first merged intersection pixel encountered during the tracking. Record all the pixels in a specific fracture trace. The tracking process is implemented on all merged intersection pixels. The red lines marked in Fig. 2(d) are the results of the tracking.

Fig. 1 presents a flow chart of the fracture detection algorithm for a clear demonstration. By recording all pixels in a specific fracture trace, we can capture the fracture curvature by representing the fracture with a polyline (Fig.2(d)). The degree of a polyline in each fracture can be decided as required, and the maximum degree is the number of pixels in the fracture trace. The most troublesome part of tracking the trace of a fracture in **Step 3** is to find the correct pixel when encountering an intersection pixel. Three steps are implemented in the algorithm. First, find the closest merged interaction pixel, and the algorithm searches for possible pixels at a given distance (the pixels intersecting the yellow box in Fig. 2(c)). Second, the algorithm finds the pixel which fits best the trend of the trace. Third, if the pixel found in the second step does not deviate significantly from the trend, this pixel is selected as the next pixel. Otherwise, the tracking stops for this trace and the current intersection pixel links to its closest merged intersection pixel. In this case, the trace is constrained

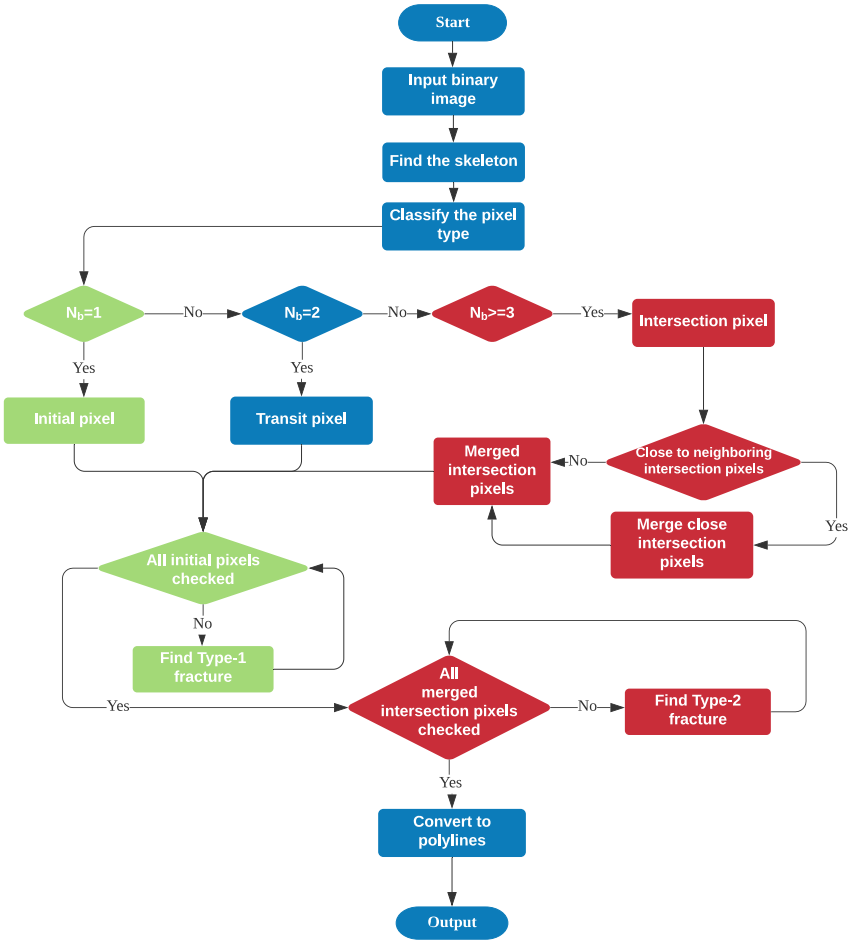

Figure 1. Flow chart of the fracture detection algorithm. N_b is the number of neighboring pixels.

by an initial pixel and a merged intersection pixel. The current intersection pixel is the isolated intersection pixel mentioned in **Step 3**. The deviation criterion is adjustable for different outcrop maps, and the size of the yellow box is dynamically adjusted from 1 to 3-pixel lengths. Similar procedures are applied to track the trace of a fracture constrained by a pair of merged intersection points.

The process to find the next pixel can also be used to find branches originating from one merged intersection pixel, where the number of branches defines the T-type and X-type intersections. If the number of branches is two or three, the corresponding merged intersection pixel is a T-type intersection. When the number of branches is two, the merged interaction pixel is a V-type intersection, where two tips coincide. Here, we do not distinguish these two types and regard both of them as T-type intersections because the probability of a V-type interaction occurring in a natural network is negligible [*Sanderson and Nixon*, 2015]. When

the number of branches is more than three, the corresponding merged intersection pixel is an X-type intersection. T-type and X-type intersections are used for topological analysis in the next section.

Fig. 3 shows one example of the digitized outcrop maps from the Achnashellach Culmination field area (Fig. 7B and 7D in [*Watkins et al.*, 2015]). Detected fracture traces are overlapped with the original outcrop map in Fig. 2(c), which shows accurate detection results. The synthetic analysis of geometric properties and topological structures of fractures are obtained with digitized outcrop maps and presented in the following section.

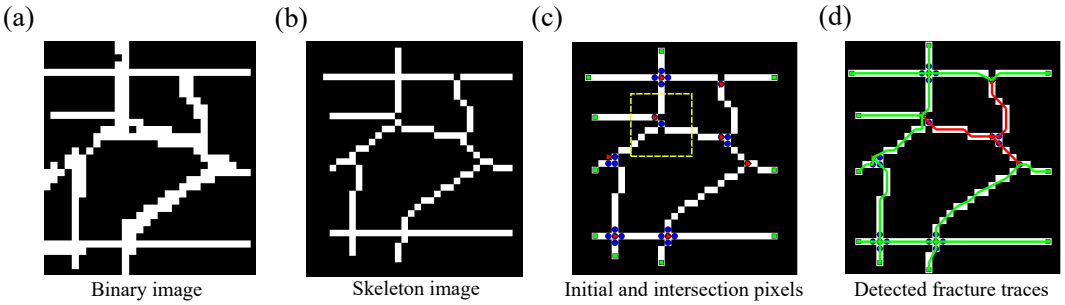

Figure 2. (a) A binary fracture map; (b) Skeleton image of the binary fracture map in (a); (c) Initial and intersection pixels of the skeleton image; Green squares represent initial pixels. Blue circles represent intersection pixels. Red triangles represent merged intersection pixels. (d) Fracture traces interpreted with our detection algorithm; The green line segments are the traces found in **Step 3** (Type 1 fracture), and the red line segments are the traces found in **Step 4** (Type 2 fracture).

3 Synthetic analysis of fracture geometries and topological structures

We implement the fracture detection algorithm on 80 published outcrop maps [*Duffy et al.*, 2017; *Prabhakaran et al.*, 2021; *Bertrand et al.*, 2015; *Thiele et al.*, 2017; *Odling*, 1997; *Jafari*, 2011; *Gillespie et al.*, 1993; *Segall and Pollard*, 1983b; *Holland et al.*, 2009; *Bisdom*, 2016; *Barton*, 1995; *Watkins et al.*, 2015; *Healy et al.*, 2017; *Becker et al.*, 2018; *Odling et al.*, 1999; *Wyller*, 2019]. These outcrop maps are collected from different parts of the world as shown in Fig. 4 and they have a wide range of scales from millimeters to tens of kilometers. Their geometric patterns are summarized and analyzed in detail, including fracture lengths, orientations, intensities and topological structures.

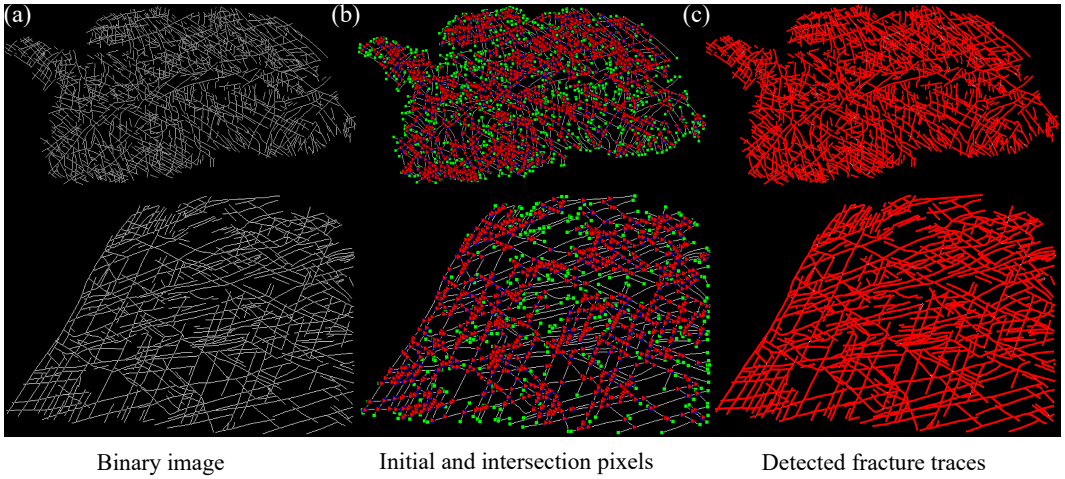

205 **Figure 3.** Digitized fracture outcrop map at Achnashellach Culmination field area (Fig. 7B and
206 7D in [*Watkins et al.*, 2015])

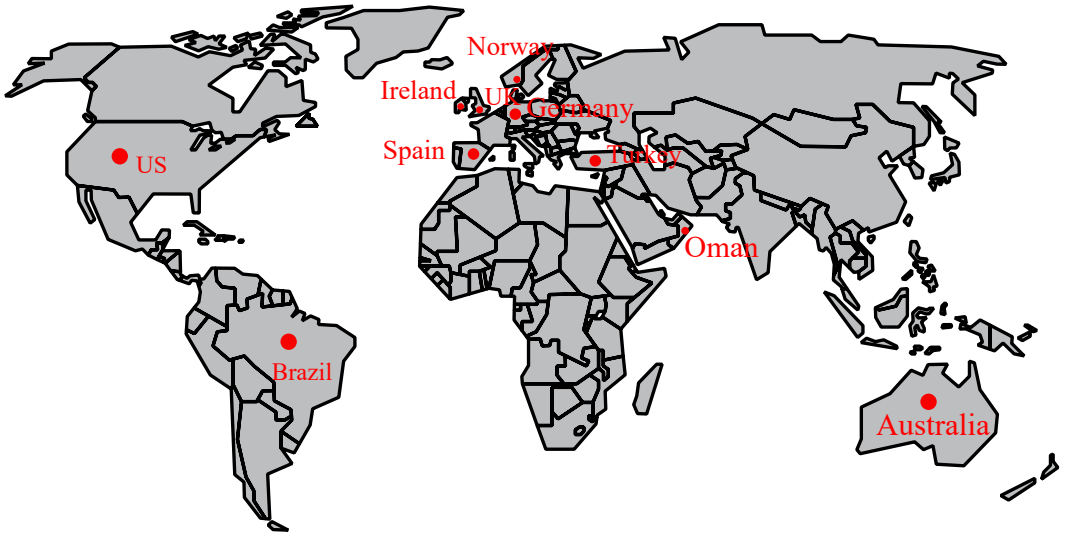

208 **Figure 4.** A world map showing locations of collected outcrops

217 ### 3.1 Length distribution

218 Exponential, log-normal and power-law distribution are usually adopted to describe
219 fracture length, and power-law distribution is prevalent [*Segall and Pollard*, 1983a; *Sornette*
220 *et al.*, 1993]. However, an in-depth explanation of the origin of power-law distribution is
221 insufficient [*Davy et al.*, 2013; *Sano et al.*, 1981].

222 *Makarov* [2007] found the universal fractality of solids through the process of destruc-
223 tion in load solids, which leads brittle fracture and plastic deformation to be self-similar at
224 different scales and in turn, their lengths follow a power-law distribution. However, many

experiments and outcrop observations show the opposite process, where large fractures are formed from the linkage and coalescence of numerous small, isolated fractures [*Cartwright et al.*, 1995; *Soliva and Benedicto*, 2004; *Otsuki and Dilov*, 2005]. Such linkage and coalescence happen in a wide range of scales (mm-km). *Cladouhos and Marrett* [1996] and *Olson* [2007] simulated the fracture growth and linkage process and observed a power-law distribution of fracture lengths.

Researchers also observed two-/three dimensional power-law distribution in outcrop maps [*Davy*, 1993], where the full-length distributions are separated into two/three regions and described with a power-law distribution with different exponents. A typical length distribution from the real outcrop map at Achnashellach Culmination field area (Fig. 7B in [*Watkins et al.*, 2015]) is shown in Fig. 5. For clarity, the fracture length is set as the number of pixels of each fracture trace instead of line segments after converting a fracture trace to a polyline. The cumulative length distribution shows varying slopes, and a two- or three-dimensional power-law distribution is insufficient to describe the length distribution.

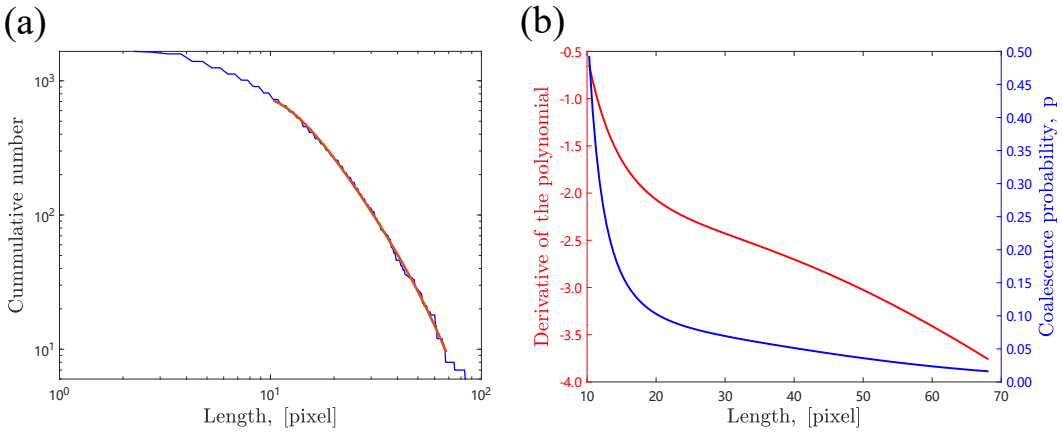

Figure 5. (a) Length distribution of outcrop maps from Achnashellach Culmination field area (Fig. 7B in [*Watkins et al.*, 2015]). The red curve is the result of a fourth-order polynomial fitting. (b) The red curve refers to the derivative of the fourth-order polynomial fitting in (a). The blue curve refers to the derived coalescence probability based on Eq. 4.

Here, we propose a simplistic model (Appendix A and B) to explain a possible origin of a power-law distribution for fracture lengths based on the self-similar characteristics of natural fractures and their coalescence. The model reproduces the iterative growth process of natural fractures, and we conclude that the fracture lengths should follow a power-law

distribution at a later generation.

$$(\frac{N_{\mathrm{N}}}{(1-p)N_0}) = (\frac{l_N}{l_0})^{\frac{\ln(p)}{\ln(n_s)}-1}, \tag{1}$$

where N_{N} is the number of fractures with a fracture length of l_N at the N^{th} generation; N_0 is the initial number of fractures; l_N is the fracture length at the N^{th} generation; l_0 is the initial length of fractures; p is the coalescence probability at each generation; n_s is the number of small fractures coalesced to form a large fracture. A simpler expression of Eq. 1 is:

$$N_N \sim l_N^{-a}, \tag{2}$$

where $a = 1 - \frac{\ln(p)}{\ln(n_s)}$.

The coalescence probability varies between 0 and 1 and the number of coalesced small fractures n_s usually varies between 2 and 5 [*Cartwright et al.*, 1995; *Soliva and Benedicto*, 2004; *Otsuki and Dilov*, 2005], so $\frac{\ln(p)}{\ln(n_s)}$ term is always negative. The corresponding exponent should always be larger than 1, which is consistent with outcrop observations [*Bonnet et al.*, 2001].

If the length distribution follows a power-law distribution, the cumulative distribution function (CDF) of fracture lengths should also follow a power-law distribution

$$C_N \sim l_N^{1-a}, \tag{3}$$

If p and n_s are constant for each generation, the cumulative length distribution should be a single power-law distribution with the exponent equal to $1-a$. However, this scenario is over-idealized, and Fig. 5(a) shows a curved CDF with varying slopes. Suppose that we regard each short growth period as a straight line segment. In that case, the varying slopes indicate fracture lengths in different short segments following a power-law distribution with different values of exponents. The variation of exponents comes from variations of p and n_s.

Due to the finite range effect [*Pickering et al.*, 1995], the exponent obtained from CDF fitting is biased. We adopt the iterative method introduced in *Pickering et al.* [1995] with $1 \sim 3$ iterations to remove the majority of bias. The number of iterations is case-dependent, and usually, 3 is a good option. An intermediate range of fracture lengths is chosen for the fitting because data points of large and small fracture lengths are inaccurate. To be specific, [0.1 0.8] of the full range is selected. Large fracture trace length is usually affected by censoring effects [*Riley*, 2005; *Priest and Hudson*, 1981; *Pickering et al.*, 1995], where the trace length is less than or equal to that of an entire trace. Small fracture trace length is inaccurate because of two possible reasons. One is the incomplete sampling or truncation because of limited resolutions of the sampling method. The second one is the

misinterpretation of close and small fractures caused by the limited resolution of published outcrop maps. Therefore, an intermediate range of lengths is more appropriate for the fitting.

We fit the cumulative length distribution with a fourth-degree polynomial and get their derivatives, corresponding to $1 - a$ at each short growth period. The slope of fitted polynomials is shown in Fig. 5(b). With fracture lengths increasing, the slope gets smaller, which corresponds to a smaller value of $\ln(p)/\ln(n_s)$. If we set $n_s = 3$ and keep constant, Eq. 4 is the formula to calculate the coalescence probability at different length scales, and the corresponding values of p are shown in Fig. 5(b).

$$p = \exp(k \times \log n_s), \tag{4}$$

where k is the slope of the cumulative length distribution.

The coalescence probability decreases with increasing fracture lengths. This observation is valid for most collected outcrops (51 out of 80), indicating that large fractures are less likely to merge and form a larger fracture. The decreasing coalescence probability may attribute to the fact that relative fracture intensity is small in large fracture systems, and the stress condition required for the coalescence of large fractures is tough.

3.2 Orientation distribution

A von Mises–Fisher distribution usually describes the orientation of fractures [*Song et al.*, 2001; *Kemeny and Post*, 2003; *Whitaker and Engelder*, 2005]. If a random D-dimensional vector $\vec{x}$ follows a von Mises–Fisher distribution, the corresponding probability distribution function is:

$$p(\vec{x} \mid \vec{\mu}, \kappa) = C_D exp(\kappa \vec{\mu}^T \vec{x}), \tag{5}$$

where $C_D(\kappa)$ is

$$C_D(\kappa) = \frac{\kappa^{D/2-1}}{2\pi^{D/2} I_{D/2-1}(\kappa)}, \tag{6}$$

where I_ν denotes the modified Bessel function of the first kind at the order of ν; The parameters $\vec{\mu}$ and κ are the mean direction and concentration parameter respectively. κ controls the concentration degree of the distribution around the mean direction $\vec{\mu}$. When $\kappa = 0$, the von Mises–Fisher distribution degenerates to a uniform distribution. When κ is large, the distribution becomes very concentrated around the angle $\vec{\mu}$.

Here, we focus on the two-dimensional outcrop maps. Fig. 6 shows rose diagrams of two outcrop maps at the Achnashellach Culmination field area (Fig. 7B and 7D in [*Watkins et al.*, 2015]). Fractures with different orientations possibly belong to different fracture sets because of different stress states during the geologic history [*Laubach*, 1988; *Tuckwell et al.*, 2003]. In each fracture set, the orientation is highly concentrated and usually has a large κ value [*Kemeny and Post*, 2003]. To distinguish fracture sets on an outcrop map is nontrivial because the fracture orientation is only one of the important factors to distinguish different fracture sets and the abutting and overprinting criteria between fractures are essential as well [*Weismüller et al.*, 2020]. More importantly, the stress history and fracture orientations in the subsurface is usually inaccessible. Therefore, we regard each outcrop map as an integrated fracture system instead of investigating each fracture set. The corresponding κ values for outcrop maps in Fig. 6 are 2.3 and 2.9, respectively. The small value of κ make the orientation distribution close to a uniform distribution, which is a widely used assumption in many SDFN modelling cases [*Bour and Davy*, 1997; *Berkowitz*, 1995; *Darcel et al.*, 2003; *Zhu et al.*, 2018].

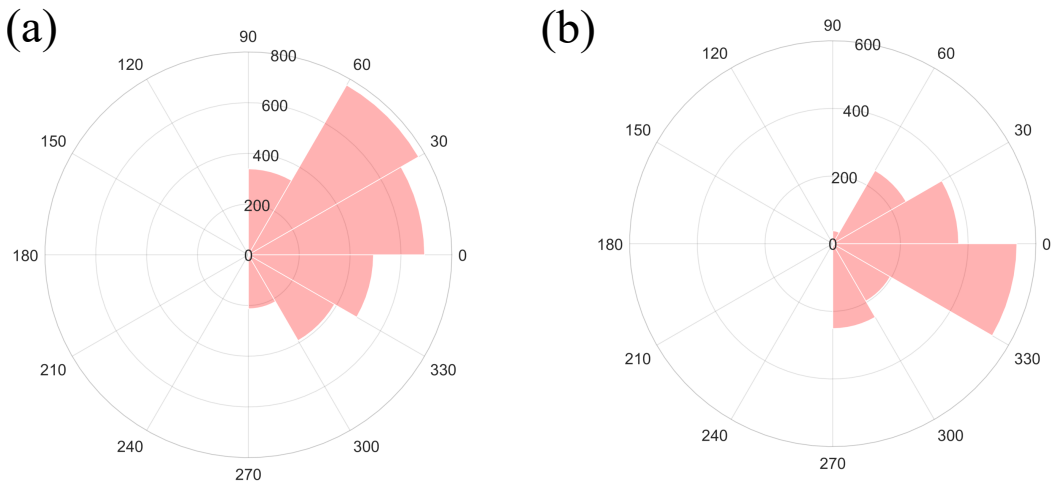

Figure 6. Orientation distribution of outcrop maps at Achnashellach Culmination field area (Fig. 7B and 7D in [*Watkins et al.*, 2015])

Summarized κ value for all 80 outcrop maps are presented versus the outcrop scale in a double-log scale in Fig. 7(a). Most small-scale outcrop maps have their orientations scattered and yield a small κ value ($\kappa < 3$), which indicates that fracture systems may be composed of many fracture sets with different orientations. Large outcrops tend to have more concentrated orientations, and the largest outcrop has the most concentrated orientation with $\kappa = 100.2$. The correlation coefficient between the outcrop scale and κ in a double-

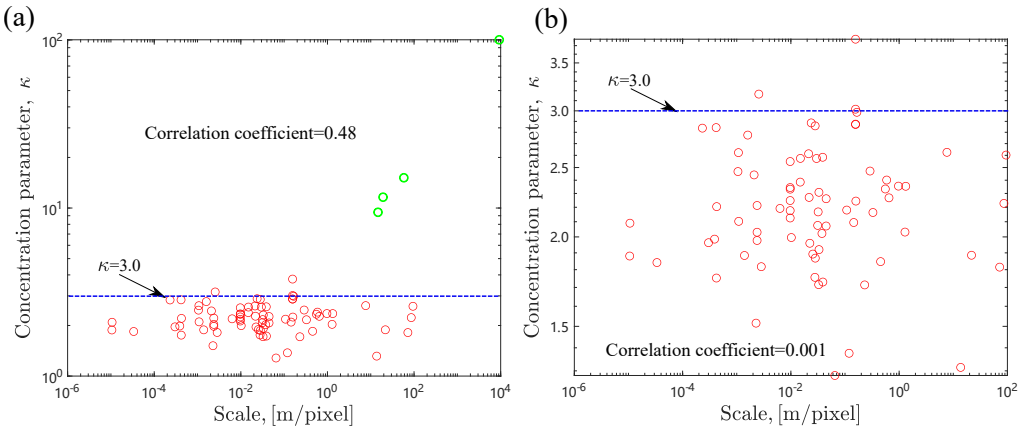

Figure 7. (a) Concentration parameters, κ, of 80 published outcrop maps; (b)Concentration parameters, κ, of 76 published outcrop maps by removing four anomalous data points (green points in (a))

log scale is 0.48, implying a positive correlation between these two parameters.However, the positive correlation is mainly caused by four anomalous data points (large-scale faults), which are marked in green. Fig. 7(b) shows κ values after removing four anomalous data points, and the correlation coefficient is close to zero. Usually, it is difficult to collect outcrop maps at large scales, which makes outcrop maps of large faults insufficient. With available datasets in this research, large faults tend to have concentrated orientations. If this trend is valid in reality, it can partially explain the small coalescence probability of large fractures because they are concentrated in orientations and are difficult to intersect each other.

3.3 Fracture intensity

Natural fractures are not uniformly distributed, but spatially clustered [*Darcel et al.*, 2003; *Zhu et al.*, 2018]. Commonly used methods to measure the spatial clustering of fracture networks include one-dimensional sampling, which measures the spacing between fractures in a given fracture set or two-dimensional sampling, which maps fracture traces exposed on the outcrop. Here we adopt the two-dimensional sampling. We divide outcrop maps into small boxes and calculate the fracture intensity in different boxes to measure the spatial clustering of the fracture network. The box intensity is defined as:

$$P_{21}^{i} = \frac{L_i}{A_i}, \tag{7}$$

where P_{21}^{i} follows the notation of fracture intensity proposed by *Dershowitz et al.* [1992], and it means the length of fracture traces per unit area in the box i; L_i is the total length of fracture traces in the box i; A_i is the area of the box i. The box size should choose

properly. If the box size is too small (Fig. 8a), the detailed structure of a fracture network is captured, but the void space between fractures are uncovered, so the spatial clustering cannot be measured. If the box size is too large (Fig. 8c), then the domain is over-averaged, and spatial variations of box intensities are insignificant. A proper box size can make most void space inside the fracture network covered, and the spatial variations of box intensities are preserved. Through trial and error, 30 pixels is a proper box size for most outcrop maps in this research, and one example is shown in Fig. 8b.

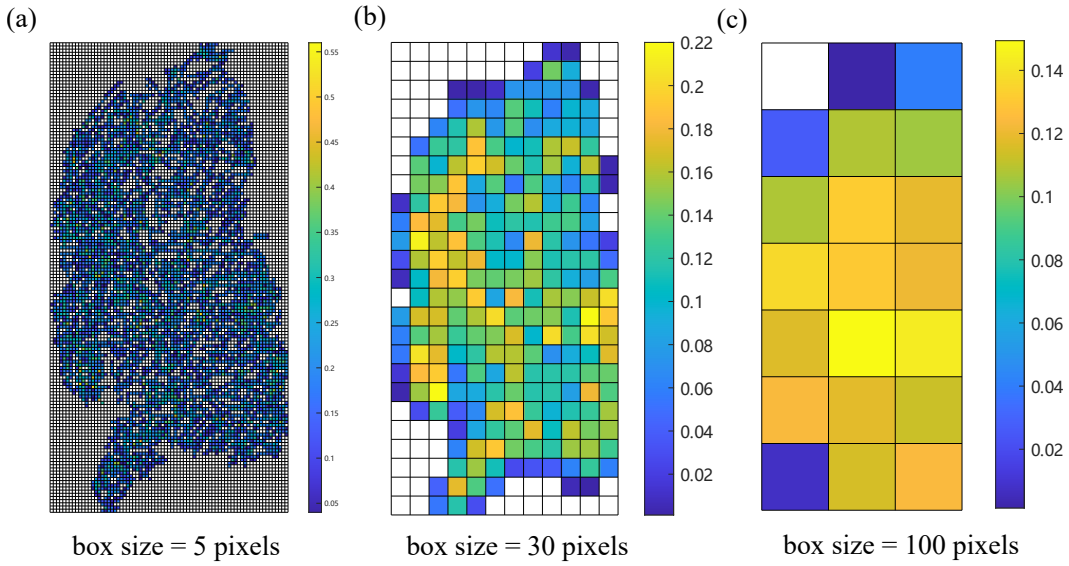

Figure 8. Box intensities of fracture outcrop map at Achnashellach Culmination field area (Fig. 7B in [*Watkins et al.*, 2015]) with different box sizes

The spatial variations of the box intensity reveal the spatial clustering of fractures. We use the coefficient of variation (CV) to measure the spatial clustering of a fracture network.

$$\mathrm{CV} = \frac{\sigma}{\mu}, \tag{8}$$

where σ is the standard deviation of box intensities; μ is the mean value of box intensities.

For a few outcrop maps with sparse fractures, boxes with a size of 30 pixels cannot cover the most void space and 100 pixels is a better choice for the box size. However, CV values calculated for those outcrop maps with box sizes of 30 and 100 pixels are close. Therefore, we take a box size of 30 pixels for all outcrop maps in this research. Fig. 9 presents the compilation of all CV values for 80 published outcrop maps. The correlation coefficient between CV and the scale is almost 0, indicating that spatial clustering can exist in all fracture networks regardless of the scale. The maximum, minimum, and mean values

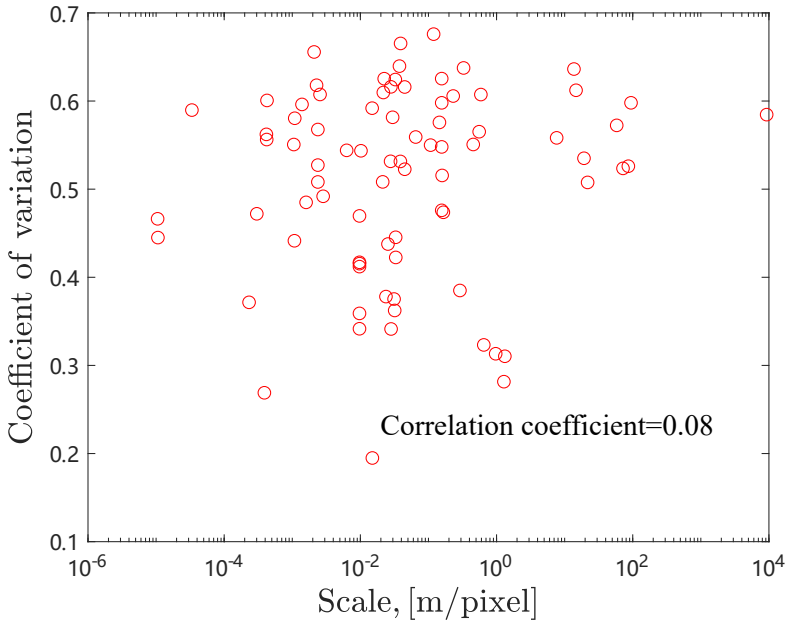

339 **Figure 9.** The coefficient of variations of box intensities of all 80 published outcrop maps

347 of CV are 0.68, 0.20 and 0.51, receptively. The standard deviation of CV is 0.1, implying
348 an insignificant variation of CV in different outcrop maps.

349 Spatial clustering can be attributed to impacts of all types of fracture geometries,
350 such as fracture positions, lengths and orientations. It is difficult to separate contributions
351 from each factor. To focus on the impact of fracture positions, we generate two stochastic
352 fracture networks with their fracture centers following a fractal and uniform spatial density
353 distribution, respectively. We keep the other geometric parameters the same and investigate
354 the spatial distribution of their box intensities. Fig. 10 (a) and (b) show the two stochastic
355 fracture networks and their box intensities are shown in Fig. 10 (c) and (d). These two
356 fracture networks have their lengths follow a power-law distribution with the exponent equal
357 3.0, and orientations follow a von Mises-Fisher distribution with $\kappa = 1.5$. The CV values for
358 the two fracture networks are 0.26 and 0.65, receptively. The fracture network with uniform
359 distributed fracture centers has the CV smaller than most outcrop maps. In contrast, the
360 fracture network with clustered center positions has a much larger CV and is closer to
361 reality. This observation suggests that natural fracture networks may have clustering effects
362 caused by their clustered positions. However, fracture lengths and orientations may have
363 significant impacts on CV as well. Therefore, more detailed and strict variable control
364 should be implemented in future research to evaluate each geometric parameter's impact
365 comprehensively.

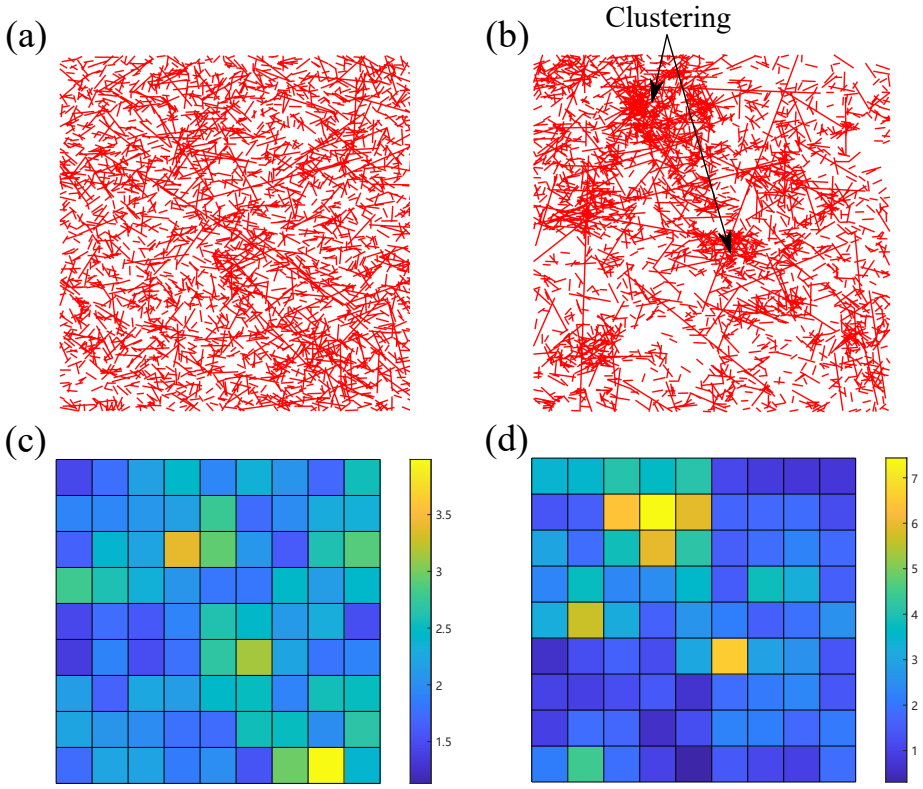

366 **Figure 10.** (a) and (b) are examples of stochastic discrete fracture networks generated by in-
367 house DFN modelling software, HatchFrac. (c) and (d) are box intensities of fracture network
368 (a) and (b), respectively. Two stochastic discrete fracture networks have their lengths follow a
369 power-law distribution with the exponent of 3.0. Fracture orientations follow a von Mises–Fisher
370 distribution with $\kappa = 1.5$. Positions of fracture centers follow a uniform (left) and fractal (right)
371 spatial density distribution receptively. The fractal dimension used in the right subfigure is 1.8.
372 The termination criterion is the formation of a spanning cluster, which connects four sides of the
373 domain.

374 ### 3.4 Topological structures

375 Fracture connectivity is essential for fluid flow in complex fracture networks, and it de-
376 pends on fracture lengths, orientations, and fracture intensities [*Zhu et al.*, 2021a]. However,
377 topology analysis can bring more insights on the connectivity compared with individual ge-
378 ometrical parameters [*Sanderson and Nixon*, 2015]. *Barton and Hsieh* [1989] introduced a
379 ternary diagram to characterize connectivity, on which the relative frequencies of the three
380 node types present in a system are plotted as a point. In this research, fracture apertures are
381 not considered; therefore, a ternary diagram is sufficient to describe topological structures

of fracture networks. The three node types include isolated tips (I-type), crossing fractures (X-type), and abutments or splays (T-type). Following *Sanderson and Nixon* [2015], we adopt C_B, the average number of connections per branch, as the measure of connectivity.

$$C_B = \frac{3 \times N_T + 4 \times N_X}{N_B}, \tag{9}$$

where N_T is the number of T-type nodes; N_X is the number of X-type nodes; and N_B is the number of branches, which is calculated by:

$$N_B = \frac{1}{2}(N_I + 3N_T + 4N_X), \tag{10}$$

where N_I is the number of I-type nodes.

C_B is a dimensionless number varying between 0 and 2, and a larger value indicates better connectivity. Fig. 11 (a) presents the ternary diagram of all 80 outcrop maps, and the colour map refers to the connectivity index C_B. The contour line of C_B is denoted in the figure.

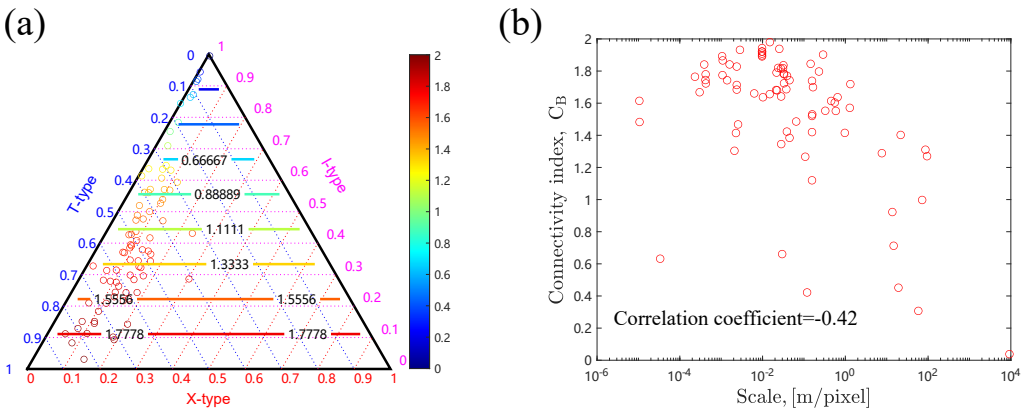

Figure 11. (a) Ternary diagram of three types of nodes, I-type, T-type and X-type; The contour lines of C_B are shown in different colors. (b) Connectivity indexes of all 80 published outcrop maps

Fracture networks with a higher proportion of T-type and X-type nodes have better connectivity. Most natural outcrops have good connectivity because their C_B value is significant. More importantly, most natural fracture networks have a large proportion of T-type nodes. T-type nodes are essential to improve the connectivity of a natural fracture system [*Dershowitz and Einstein*, 1988; *Barton and Hsieh*, 1989; *Odling*, 1997], because a high proportion of T-type nodes can lead to fewer dead-ends within each connected cluster. Fig. 11 (b) shows the plot between the connectivity index C_B and the scale. The correlation coefficient is -0.42, indicating a moderate negative correlation between these two parameters.

Large scale fracture networks usually have weaker connectivity compared with small-scale fracture networks under the data collection in this research. One crucial factor is that large fracture systems are more likely to have concentrated orientations, as discussed in the previous section on fracture orientations. Such concentrated orientations make large fractures difficult to link each other and form more complex and better-connected fracture networks.

3.5 Clusters and flow analysis

Topological analysis can quantify the connectivity of fracture networks but cannot explicitly demonstrate the flow pathways. Fluid flow happens in connected instead of isolated fractures for low permeability formations; therefore, it is necessary to check clusters in outcrop maps. With the DFN modelling software, HatchFrac [*Zhu et al.*, 2019, 2021a], we can check and label clusters of those outcrop maps after the digitization. Fig. 12 shows different clusters in outcrop maps from Spireslack open cast coal pit, south of Glasgow in Scotland (Fig. 7 in *Healy et al.* [2017]). We use different neighbouring colours to distinguish different clusters. In Fig. 12, no spanning cluster is formed. A spanning cluster connects all boundaries of the outcrop map. Local clusters have different sizes and yield good local instead of global connectivity. Fig. 13 shows clusters in outcrop maps at Achnashellach Culmination field area (Fig. 7B and 7D in *Watkins et al.* [2015]). Spanning clusters are formed in both outcrop maps, which are marked in red. 63 out of 80 natural outcrop maps have formed a spanning cluster, and this percentage is higher for small-scale outcrop maps, indicating good global connectivity of fracture networks in outcrop maps.

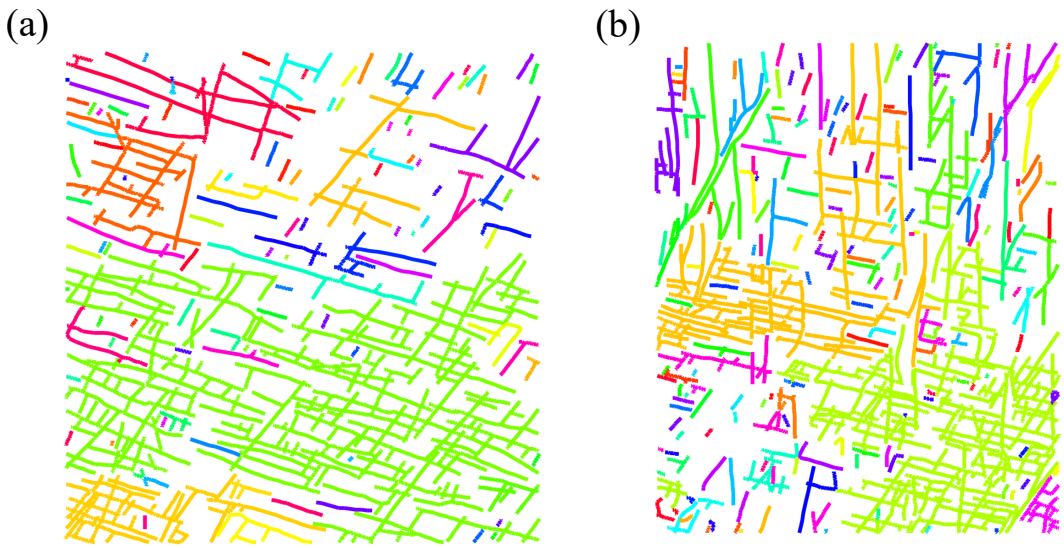

Figure 12. Fracture outcrop map at the Spireslack open cast coal pit, south of Glasgow in Scotland (Fig. 7 in *Healy et al.* [2017]). Different colors are applied to distinguish different clusters.

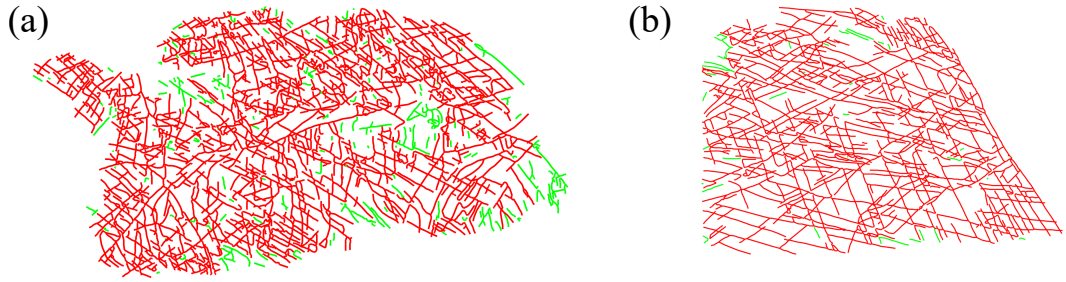

Figure 13. Fracture outcrop map at Achnashellach Culmination field area (Fig. 7B and 7D in *Watkins et al.* [2015]). Red line segments are the largest spanning cluster; Green line segments are local clusters.

If all fractures are open and have a large aperture, fractures in the spanning cluster can provide a highly permeable pathway for any fluid flow. However, over geologic time, compression and cementation can cause the closure and sealing of fractures, which together significantly reduce the fracture permeabilities [*Ito and Zoback*, 2000; *Im et al.*, 2018]. Under today's stress field or having severe stress perturbation, such as hydraulic fracturing, critically orientated fractures can be critically stressed and slide [*Barton et al.*, 1995]. Sliding of critically stressed fractures induces shear displacement and enlarges the fracture aperture because of roughness [*Yeo et al.*, 1998; *Kim and Inoue*, 2003]. Non-critically stressed fractures are probably sealed and impermeable after a long geological history. In Fig. 14, we assume the principal stress $S_1 = 1$ as the reference, with the orthogonal principal stress $S_2 = 0.6S_1$ and pore pressure $P_p = 0.5S_1$. The Coulomb failure criterion [*Coulomb*, 1773] is adopted for simplicity to distinguish critical and non-critical stressed fractures [*Im et al.*, 2018; *Mattila and Follin*, 2019; *Evans*, 2005]:

$$\tau = \mu(S_n - P_p), \tag{11}$$

where μ is the coefficient of friction along the fracture plane, P_p is local pore pressure, and τ and S_n are respectively shear and normal stresses on a fracture.

In Fig. 14, red fractures are critically stressed and highly permeable due to sliding; blue fractures are mechanically stable and non-permeable because of sealing. Non-critically stressed fractures could also be partially sealed and yield complex sealing patterns. However, this is out of the scope of this research, and relevant results can be found in our previous [*Zhu et al.*, 2021b] and future researches. The stress state of each fracture is shown in a Mohr's diagram in Figs. 14(c,d). Red crosses refer to stress states of critically stressed fractures, and blue dots are stress states of mechanically stable fractures.

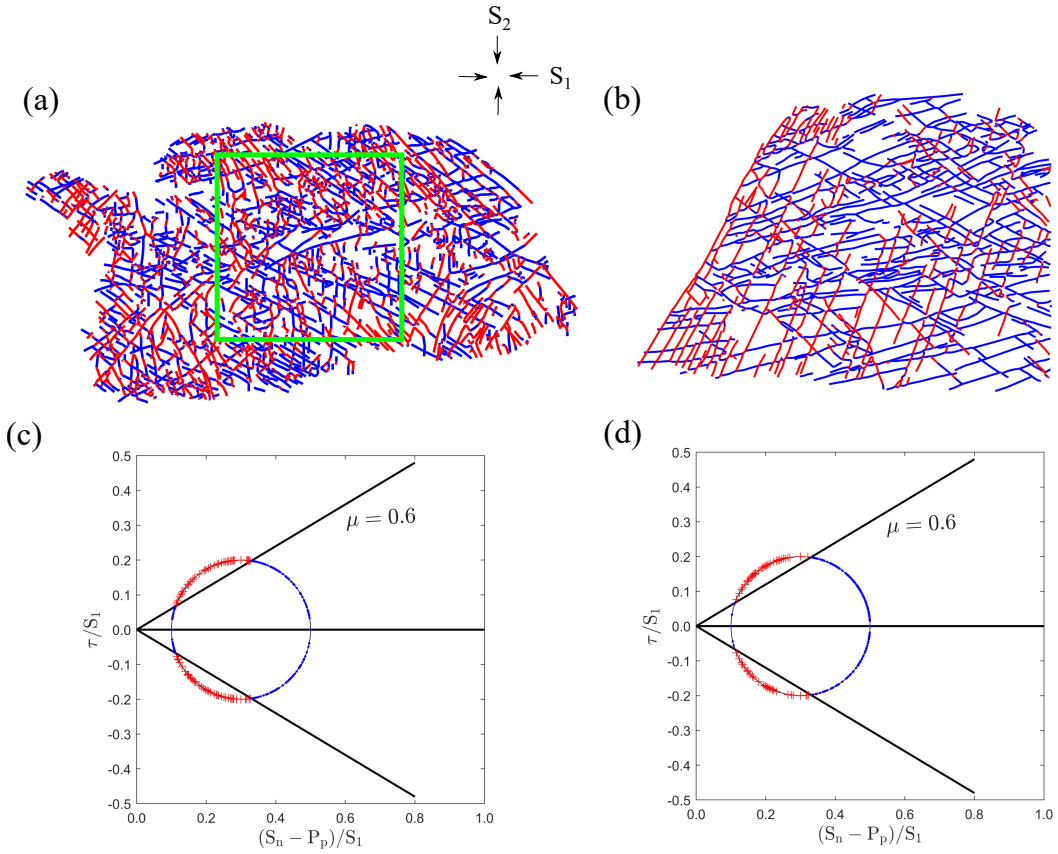

Figure 14. Fracture outcrop map at Achnashellach Culmination field area (Fig. 7B and 7D in *Watkins et al.* [2015]). Red line segments are critically stressed fractures and blue line segments are mechanically stable fractures. The stress state of each fracture plane is shown in the Mohr's diagram. The subdomain (green square) is selected for the flow simulation.

To explicitly demonstrate the impact of fractures on the formation permeability, we implement a full-scale, embedded discrete fracture matrix simulation with UNCONG simulator [*Li et al.*, 2015] and calculate the formation permeability in different scenarios. We cut a square subdomain (green square) from Fig. 14(a) for a convenient implementation, and the size of the subdomain is set as 100 $m \times 100$ m. We prescribe a constant pressure boundary condition, where the pressure at the inflow boundary (the left-hand side) is set to 2 bar, and all the other boundaries (the remaining three sides) have zero bar. The pressure difference yields a macroscopic pressure gradient of 2 kPa/m, which constrains the Reynolds number to a realistic range, $\mathcal{O}(10^{-3})$. The upper and lower boundary are impermeable. The matrix has a permeability of 0.1 mD since we are considering a low permeability formation. Critically stressed fractures are assumed to have an aperture of 500 micrometers, which yield a permeability of 20,833 mD based on the cubic law [*Kochina et al.*, 1962]. Three sce-

narios are considered to demonstrate the impact of fractures on the formation permeability: i. no fractures; ii. critically stressed fractures have a permeability of 20,833 mD, and non-critically stressed fractures are impermeable (Fig. 15(a)); iii. both critically stressed and non-critically stressed fractures have a permeability of 20,833 mD (Fig. 15(b)). We set the formation permeability of the first scenario as the reference $K_{\text{ref}} = 1$. The pressure distribution of three scenarios are presented in Fig. 15(c-e). If all fractures are highly permeable, fractures can significantly increase the formation permeability by 362%. However, if only critically stressed fractures are permeable, then the increase is only 8% and insignificant. Although the topological connectivity of the fracture network in the chosen subdomain is good, hydraulic connectivity is not guaranteed. Fractures can be essential for fluid flow in low permeability formations. However, their impacts still depend on many factors, including topological connectivity, sealing patterns, global and local stress conditions.

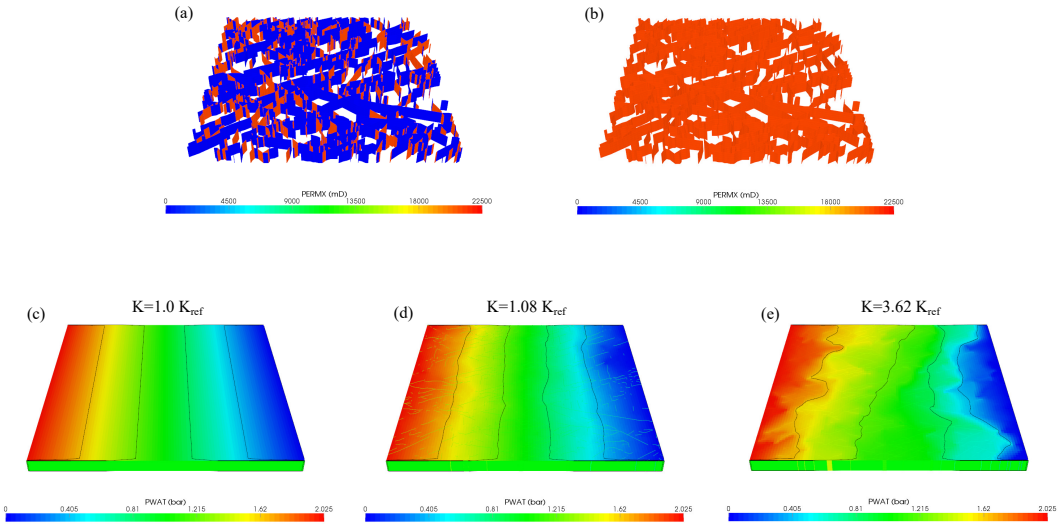

Figure 15. (a) Fracture permeability with stress impact; (b) Fracture permeability without stress impact (all fractures are open); (c-e) pressure distribution of the formation in different scenarios: (c) no fracture; (d) critically stressed fractures have a permeability of 20,833 mD, and non-critically stressed fractures are impermeable; (e) both critically stressed and non-critically stressed fractures have a permeability of 20,833 mD.

4 Discussions

Through digitizing published natural outcrop maps with the pixel-based fracture detection algorithm, we systematically investigate geometric patterns of fractures, including fracture lengths, orientations, fracture intensities and topological structures. The geometric

patterns are essential for discrete fracture network modelling since the critical strategy of SDFN modelling is to describe fracture geometries with stochastic distributions. The validation of such discrete fracture networks is impossible because the comprehensive information about the subsurface structures is inaccessible with current technologies. The confidence of SDFN models thus depends on the justification of chosen stochastic distributions.

A power-law distribution usually describes fracture lengths. However, this research shows that fracture lengths may not follow a single power-law distribution but multiple power-law distributions with varying exponents. The simplistic model we proposed explains a possible origin of the power-law distribution concerning fracture growth and linkage. The derived power-law exponents of fracture lengths are larger than 1, consistent with most outcrop observations. Two parameters adopted in the simplistic model, the coalescence probability and the number of coalesced minor fractures, can successfully explain the variation of power-law exponents for fractures with different lengths. The exponent is usually large for long fractures, possibly attributed to a small coalescence probability caused by concentrated orientations, sparse fractures and high requirements on stress conditions.

Over a long geologic history of subsurface rocks, varying stress states can generate fracture sets with different orientations. Each fracture set has concentrated orientations, thus has a large κ value. However, the stress history is hardly known, and most SDFN models regard all sets of fractures belong to an integrated fracture system and describe their orientations with a uniform distribution. From observations in this paper, most small-scale fracture systems ($< 100\ m$) have their orientation distribution closer to a uniform distribution. The corresponding concentration degree κ is smaller than 3 in a von Mises–Fisher distribution. However, large fracture systems usually have more concentrated orientations with a large κ value as observed in the collected datasets in this research. A positive correlation exists between the scale and concentration degree (κ). Concentrated orientations of large fracture systems usually make them difficult to intersect and merge, thus make large fractures have a small coalescence probability.

Fracture intensities are not spatially uniform but clustered. Spatial clustering can improve the local connectivity but hardly contribute to the global connectivity [*Zhu et al.*, 2018]. Such spatial clustering can exist in all fracture networks regardless of scales, possibly attributed to fracture lengths, orientations and fracture positions. Evaluating the impact of each geometric parameter on spatial clustering needs more strict variable control and detailed investigations, which is beyond the scope of this paper and will be discussed in future research. A fractal spatial density distribution generates clustered positions and significantly increase the spatial clustering of the system. Therefore, a fractal spatial density

distribution can better capture the spatial clustering of fracture systems compared with a uniform spatial density distribution.

The topological analysis finds that most natural fracture networks have a significant proportion of T-type nodes and good connectivity. However, commonly adopted SDFN models cannot generate T-type nodes but only X-type and I-type nodes. A random truncation of branches at X-type nodes to form T-type nodes is undesirable for developing realistic fracture networks, because the abutment relationship reveals the growth history of fractures. Therefore, it is necessary to mimic the fracture growth process and form T-type intersections. Detailed numerical simulation based on fracture mechanics is inapplicable for discrete fracture networks with massive fractures. Rule-based fracture growth process [*Davy et al.*, 2013] is more appropriate for the implementation. Rules, such as nuclei distributions, growth criteria, growth velocities, and termination criteria, can be summarized from classic theories, experiments, and numerical simulations. Then, growth rules can be incorporated in an SDFN model at each time step to mimic the growth process.

Furthermore, 63 out of 80 natural outcrop maps have formed a spanning cluster, indicating good global connectivity of exposed fracture networks. However, fracture networks in the subsurface are three-dimensional. Outcrops are only cross-section maps of the corresponding 3D structures with the ground as the cross-sectional plane. If the rock types and structural settings of the surface outcrops and subsurface formations are similar, outcrops can be regarded as relevant to the subsurface formation. However, weathering, stress-release during the upward movement and complex surface topography can cause outcrops to differ from the subsurface systems significantly [*Ukar et al.*, 2019]. Therefore, 2D outcrop maps cannot completely characterize the real subsurface fracture networks. The correlation between the connectivity in 2D and 3D will be systematically investigated in the near future. In 2D outcrop maps, good topological connectivity (formation of the spanning cluster) cannot ensure good hydraulic connectivity because fracture permeability can be significantly reduced, attributing to the compression and sealing. Therefore, considering sealing patterns and global and local stress states is necessary to evaluate the flow contribution from fractures in low permeability formations.

In a nutshell, several improvements listed above are available for current stochastic discrete fracture network models to be more representative.

5 Conclusions

We have analyzed fracture geometries in detail with 80 published outcrop maps. The findings and observations from this research are essential to construct a representative dis-

crete fracture network, and a meaningful DFN model is a premise for investigations of complex flow behaviours in the subsurface. The key conclusions from our research are:

- A pixel-based fracture detection algorithm can interpret binary outcrop maps as polylines. The algorithm is robust, accurate and efficient.
- For most outcrop maps, fracture lengths follow multiple power-law distributions instead of a single one. Our simplistic model successfully explains a possible origin of the multiple power-law distributions, attributing to variations of the coalescence probability, p, and the number of coalesced fractures, n_s, at different generations. Large fractures usually have large exponents, possibly because of a small coalescence probability.
- Natural fracture systems are usually composed of many fracture sets with different orientations, which results in small κ values in a von Mises–Fisher distribution. Most small-scale fracture systems have their concentration parameter κ smaller than 3. Large fracture systems usually have more concentrated orientations with large κ values.
- Fracture intensities are usually spatially clustered instead of uniformly distributed in fracture systems at all scales. A fractal spatial density distribution can better capture spatial clustering through generating clustered fracture positions.
- Natural fracture networks are usually well connected with a significant proportion of T-type intersections. However, the conventional DFN modelling method cannot generate T-type intersections. Thus, developing a rule-based algorithm, which mimics fracture growth and forms T-type nodes, is necessary.
- Most natural outcrop maps form a spanning cluster, indicating good topological connectivity. However, good topological connectivity cannot ensure good hydraulic connectivity of fracture networks in the outcrop map. Compression and sealing over geological time can significantly reduce fractures' permeability. However, current stress states or stress perturbations (like hydraulic fracturing) can essentially change the mechanical state of fractures and their permeability and must be included to evaluate the impact of fractures on the subsurface flow.
- 2D outcrops can only be regarded as cross-section maps of 3D subsurface fracture networks after experiencing server weathering and stress-release. More researches are necessary to link the properties, such as fracture intensity and connectivity, in different dimensions.

Acknowledgments

This project was supported by the National Key Research and Development Program of China (No. 2019YFA0708704). The authors would like to thank all editors and anonymous reviewers for their comments and suggestions. All the synthetically generated data and digitized outcrop maps are available online (`https://doi.org/10.4121/14865096.v2`)

A: A simplistic model

We propose a simplistic model to demonstrate a possible origin of the power-law distribution of fracture lengths. The basic assumptions are listed:

- Initial fractures are small fractures with constant length, l_0, and the number of initial fractures is N_0;
- Large fractures grow from the coalescence of small fractures. n_s is number of small fractures, which coalesce and form one large fracture;
- The length of coalesced fracture equal $n_s \times l_{i-1}$. The overlapping and underlapping structures are ignored;
- A constant coalescence probability, p, applies on each generation and decides the number of small fractures coalesced to form large fractures in each generation.
- At the i^{th} generation, $\frac{N_{i-1} \times p}{n_s}$ fractures will coalesce and form the i^{th} generation fractures with length l_i. The number of remained fractures at the $i-1$ generation is denoted as $N_{i-1(remain)}$ and those fractures are observable with length l_{i-1}, which is equal to $N_{i-1} \times (1-p)$

At the initial state ($n = 0$), we have

$$\begin{cases} N_0 = N_0 \\ l_0 = l_0 \end{cases} \tag{A.1}$$

At the first generation, $n = 1$

$$\begin{cases} N_1 = \frac{N_0 \times p}{n_s} \\ l_1 = n_s l_0 \\ N_{0(remain)} = N_0(1-p) \end{cases} \tag{A.2}$$

where $N_{0(remain)}$ is the remained fractures at the initial state.

At the second generation, $n = 2$

$$\begin{cases} N_2 = \frac{N_1 \times p}{n_s} = (\frac{p}{n_s})^2 N_0 \\ l_2 = n_s^2 l_0 \\ N_{1(remain)} = N_1(1-p) = \frac{N_0 \times p}{n_s}(1-p) \end{cases} \tag{A.3}$$

At the N^{th} generation, $n = N$

$$\begin{cases} N_N = \frac{N_{N-1} \times p}{n_s} = (\frac{p}{n_s})^N N_0 \\ l_N = n_s^N l_0 \\ N_{N-1(remain)} = N_{N-1}(1-p) = (\frac{p}{n_s})^{N-1}(1-p)N_0 \end{cases} \tag{A.4}$$

Take the logarithm of the first two equations in Eqs.(4), we have

$$\begin{cases} \ln(\frac{N_N}{N_0}) = N \ln(\frac{p}{n_s}) \\ \ln(\frac{l_N}{l_0}) = N \ln(n_s) \end{cases} \tag{A.5}$$

Therefore, we have

$$\ln(\frac{N_N}{N_0}) = \ln(\frac{l_N}{l_0}) \ln(\frac{p}{n_s}) / \ln(n_s) \tag{A.6}$$

which is equal to

$$\ln(\frac{N_N}{N_0}) = \ln\{(\frac{l_N}{l_0})^{\ln(\frac{p}{n_s})/\ln(n_s)}\} \tag{A.7}$$

Therefore,

$$(\frac{N_N}{N_0}) = (\frac{l_N}{l_0})^{\frac{\ln(p)}{\ln(n_s)}-1} \tag{A.8}$$

Therefore, we see that the length of fractures at different generations (or different scales) follow a power-law distribution, and the exponent should be smaller than -1 (when p equals 1).

However, what we observe in reality is the remained fractures. With the similar procedures, the number of fractures remained at the N^{th} generation follow a power law distribution.

$$\frac{N_{N(remain)}}{(1-p)N_0} = (\frac{l_N}{l_0})^{\frac{\ln(p)}{\ln(n_s)}-1} \tag{A.9}$$

Since both N_N and $N_{N(remain)}$ follow a power-law distribution with the same exponent, but different coefficients, we do not distinguish these two parameters and denote the number of fractures with length l_N as N_N for the following discussion.

- When $p = 0$, which corresponds to the initial state, we have

$$(\frac{N_N}{N_0}) = (\frac{l_N}{l_0})^{-\infty} = 0 \tag{A.10}$$

therefore, the number of all fractures larger than l_0 is zero and we only have fractures at the initial state.

- When $p = 1$, which corresponds to the case where all small fractures are coalesced to form large fractures. We have

$$(\frac{N_N}{N_0}) = (\frac{l_N}{l_0})^{-1} = \frac{l_0}{l_N} \tag{A.11}$$

therefore,

$$N_N = \frac{l_0}{l_N} \times N_0 \tag{A.12}$$

This scenario has the exponent of 1 and the number of fractures remained at all previous generations is zero.

- Because of complex stress states and interactions between fractures (such as stress shadow), the coalescence probability cannot be 1. If we take $p = 0.7$ and $n_s = 3$, we have the exponent

$$a = -(\{\ln(0.7)/\ln(3)\} - 1) = 1.32 \tag{A.13}$$

If $p = 0.3$ and $n_s = 3$, the exponent is about 2.1; If $p = 0.1$ and $n_s = 3$, the exponent is about 3.1; If $p = 0.01$ and $n_s = 3$, the exponent is about 5.9. Therefore, a larger exponent may suggest a smaller coalescence probability.

These derivations can explain why fracture lengths of different scales follow a power-law distribution and provide a possible range for the exponent $[1, \infty]$. The exponent depends on the coalescence probability and the number of coalesced fractures, but it has to be larger than 1. *Bonnet et al.* [2001] provided a compilation of power-law exponents for fracture length distributions of different outcrop maps. Only one map has their exponent equal to 0.9 (table 2 in [*Bonnet et al.*, 2001]). A possible reason is that their length measurement is inaccurate, and the fitting is not perfect because the outcrop map shows a km-scale fault system.

B: Cumulative length distribution

Furthermore, we can derive the cumulative length distribution by the integration of the length distribution.

$$C_N \sim \int_{l_{min}}^{l_N} l^{-a} dl = (1-a)\{l_N^{1-a} - l_{min}^{1-a}\} \tag{B.1}$$

therefore:

$$c_N \sim l_N^{1-a} \tag{B.2}$$

where $a = \frac{\ln(p)}{\ln(n_s)} - 1$

From collected length data, we can see that the cumulative length distribution does not follow a single power-law distribution but multiple power-law distributions. The exponents become larger when fracture lengths increase. The larger exponent means a smaller coalescence probability. Therefore, the coalescence probability, p, should be a function of the fracture length

$$p = p(l, others) \tag{B.3}$$

From collected data, we know $\frac{\partial p}{\partial l} < 0$.

References

Adler, P. M., and J.-F. Thovert (1999), *Fractures and fracture networks*, vol. 15, Springer Science & Business Media.

Ahmadi, H., and E. Pekkan (2021), Fault-based geological lineaments extraction using remote sensing and gis—a review, *Geosciences*, *11*(5), 183.

Andresen, C. A., A. Hansen, R. Le Goc, P. Davy, and S. M. Hope (2013), Topology of fracture networks, *Frontiers in Physics*, *1*, 7.

Barton, C., and P. A. Hsieh (1989), Physical and hydrologic-flow properties of fractures, in *28th International Geological Congress Field Trip Guidebook*, vol. 385, p. 36.

Barton, C. A., M. D. Zoback, and D. Moos (1995), Fluid flow along potentially active faults in crystalline rock, *Geology*, *23*(8), 683–686.

Barton, C. C. (1995), *Fractals in the earth sciences*, Springer.

Becker, I., B. Koehrer, M. Waldvogel, W. Jelinek, and C. Hilgers (2018), Comparing fracture statistics from outcrop and reservoir data using conventional manual and t-lidar derived scanlines in ca2 carbonates from the southern permian basin, germany, *Marine and Petroleum Geology*, *95*, 228–245.

Berkowitz, B. (1995), Analysis of fracture network connectivity using percolation theory, *Mathematical Geology*, *27*(4), 467–483, doi:10.1007/BF02084422.

Berkowitz, B. (2002), Characterizing flow and transport in fractured geological media: A review, *Advances in Water Resources*, *25*(8-12), 861–884.

Bertrand, L., Y. Géraud, E. Le Garzic, J. Place, M. Diraison, B. Walter, and S. Haffen (2015), A multiscale analysis of a fracture pattern in granite: A case study of the tamariu granite, catalunya, spain, *Journal of Structural Geology*, *78*, 52–66.

Bisdom, K. (2016), Burial-related fracturing in sub-horizontal and folded reservoirs: Geometry, geomechanics and impact on permeability.

Bisdom, K., B. Gauthier, G. Bertotti, and N. Hardebol (2014), Calibrating discrete fracture-network models with a carbonate three-dimensional outcrop fracture network: Implica-

659 tions for naturally fractured reservoir modeling, *AAPG bulletin*, *98*(7), 1351–1376.

660 Bonnet, E., O. Bour, N. E. Odling, P. Davy, I. Main, P. Cowie, and B. Berkowitz (2001),
661 Scaling of fracture systems in geological media, *Reviews of geophysics*, *39*(3), 347–383.

662 Bour, O., and P. Davy (1997), Connectivity of random fault networks following a power law
663 fault length distribution, *Water Resources Research*, *33*(7), 1567–1583.

664 Cartwright, J. A., B. D. Trudgill, and C. S. Mansfield (1995), Fault growth by segment
665 linkage: an explanation for scatter in maximum displacement and trace length data from
666 the Canyonlands Grabens of SE Utah, *Journal of Structural Geology*, *17*(9), 1319–1326.

667 Cladouhos, T. T., and R. Marrett (1996), Are fault growth and linkage models consistent
668 with power-law distributions of fault lengths?, *Journal of Structural Geology*, *18*(2-3),
669 281–293.

670 Cook, A., L. Myer, N. Cook, and F. Doyle (1990), The effects of tortuosity on flow through
671 a natural fracture.

672 Coulomb, C. (1773), Essai sur une application des regles de maximis et minimis a quelques
673 problemes de statique relatifs a 1'architecture, *Mem. Div. Sav. Acad.*

674 Darcel, C., O. Bour, P. Davy, and J. De Dreuzy (2003), Connectivity properties of two-
675 dimensional fracture networks with stochastic fractal correlation, *Water resources re-*
676 *search*, *39*(10).

677 Davy, P. (1993), On the frequency-length distribution of the san andreas fault system,
678 *Journal of Geophysical Research: Solid Earth*, *98*(B7), 12,141–12,151.

679 Davy, P., R. Le Goc, and C. Darcel (2013), A model of fracture nucleation, growth and arrest,
680 and consequences for fracture density and scaling, *Journal of Geophysical Research: Solid*
681 *Earth*, *118*(4), 1393–1407.

682 Dershowitz, W., and H. Einstein (1988), Characterizing rock joint geometry with joint
683 system models, *Rock mechanics and rock engineering*, *21*(1), 21–51.

684 Dershowitz, W. S., H. H. Herda, et al. (1992), Interpretation of fracture spacing and inten-
685 sity, in *The 33th us symposium on rock mechanics (USRMS)*, American Rock Mechanics
686 Association.

687 Dong, Y., Y. Fu, T.-C. J. Yeh, Y.-L. Wang, Y. Zha, L. Wang, and Y. Hao (2019), Equivalence
688 of discrete fracture network and porous media models by hydraulic tomography, *Water*
689 *Resources Research*, *55*(4), 3234–3247.

690 Duffy, O. B., C. W. Nixon, R. E. Bell, C. A.-L. Jackson, R. L. Gawthorpe, D. J. Sanderson,
691 and P. S. Whipp (2017), The topology of evolving rift fault networks: Single-phase vs
692 multi-phase rifts, *Journal of Structural Geology*, *96*, 192–202.

693 Dverstorp, B., J. Andersson, and W. Nordqvist (1992), Discrete fracture network interpreta-
694 tion of field tracer migration in sparsely fractured rock, *Water Resources Research*, *28*(9),

2327–2343.

Evans, K. F. (2005), Permeability creation and damage due to massive fluid injections into granite at 3.5 km at Soultz: 2. Critical stress and fracture strength, *Journal of Geophysical Research: Solid Earth*, *110*(B4).

Gertsch, L. S. (1995), Three-dimensional fracture network models from laboratory-scale rock samples, in *International Journal of Rock Mechanics and Mining Sciences and Geomechanics Abstracts*, vol. 7, p. 322A.

Gillespie, P., C. Howard, J. Walsh, and J. Watterson (1993), Measurement and characterisation of spatial distributions of fractures, *Tectonophysics*, *226*(1-4), 113–141.

He, X., M. Sinan, H. Kwak, and H. Hoteit (2021), A corrected cubic law for single-phase laminar flow through rough-walled fractures, *Advances in Water Resources*, p. 103984.

Healy, D., R. E. Rizzo, D. G. Cornwell, N. J. Farrell, H. Watkins, N. E. Timms, E. Gomez-Rivas, and M. Smith (2017), Fracpaq: A matlab™ toolbox for the quantification of fracture patterns, *Journal of Structural Geology*, *95*, 1–16.

Holland, M., N. Saxena, and J. L. Urai (2009), Evolution of fractures in a highly dynamic thermal, hydraulic, and mechanical system-(ii) remote sensing fracture analysis, jabal shams, oman mountains, *GeoArabia*, *14*(3), 163–194.

Hyman, J., S. L. Painter, H. Viswanathan, N. Makedonska, and S. Karra (2015), Influence of injection mode on transport properties in kilometer-scale three-dimensional discrete fracture networks, *Water Resources Research*, *51*(9), 7289–7308.

Im, K., D. Elsworth, and Y. Fang (2018), The influence of preslip sealing on the permeability evolution of fractures and faults, *Geophysical Research Letters*, *45*(1), 166–175.

Ito, T., and M. D. Zoback (2000), Fracture permeability and in situ stress to 7 km depth in the KTB scientific drillhole, *Geophysical Research Letters*, *27*(7), 1045–1048.

Jafari, A. (2011), Permeability estimation of fracture networks, Ph.D. thesis, University of Alberta.

Kemeny, J., and R. Post (2003), Estimating three-dimensional rock discontinuity orientation from digital images of fracture traces, *Computers & Geosciences*, *29*(1), 65–77.

Kim, H., and J. Inoue (2003), Analytical approach for anisotropic permeability through a single rough rock joint under shear deformation, *Journal of Geophysical Research: Solid Earth*, *108*(B8).

Kochina, P., et al. (1962), Theory of ground water movement.

Koike, K., S. Nagano, and M. Ohmi (1995), Lineament analysis of satellite images using a segment tracing algorithm (sta), *Computers & Geosciences*, *21*(9), 1091–1104.

Laubach, S. E. (1988), Subsurface fractures and their relationship to stress history in east texas basin sandstone, *Tectonophysics*, *156*(1-2), 37–49.

Li, X., D. Zhang, and S. Li (2015), A multi-continuum multiple flow mechanism simulator for unconventional oil and gas recovery, *Journal of Natural Gas Science and Engineering*, *26*, 652–669.

Makarov, P. (2007), Evolutionary nature of structure formation in lithospheric material: universal principle for fractality of solids, *Russian Geology and Geophysics*, *48*(7), 558–574.

Mattila, J., and S. Follin (2019), Does In Situ State of Stress Affect Fracture Flow in Crystalline Settings?, *Journal of Geophysical Research: Solid Earth*, *124*(5), 5241–5253.

Nur, A. (1982), The origin of tensile fracture lineaments, *Journal of Structural Geology*, *4*(1), 31–40.

Odling, N., P. Gillespie, B. Bourgine, C. Castaing, J. Chiles, N. Christensen, E. Fillion, A. Genter, C. Olsen, L. Thrane, et al. (1999), Variations in fracture system geometry and their implications for fluid flow in fractures hydrocarbon reservoirs, *Petroleum Geoscience*, *5*(4), 373–384.

Odling, N. E. (1997), Scaling and connectivity of joint systems in sandstones from western norway, *Journal of Structural Geology*, *19*(10), 1257–1271.

Olson, J. (2007), Fracture aperture, length and pattern geometry development under biaxial loading: a numerical study with applications to natural, cross-jointed systems, *Geological Society, London, Special Publications*, *289*(1), 123–142.

Otsuki, K., and T. Dilov (2005), Evolution of hierarchical self-similar geometry of experimental fault zones: Implications for seismic nucleation and earthquake size, *Journal of Geophysical Research: Solid Earth*, *110*(B3).

Pickering, G., J. Bull, and D. Sanderson (1995), Sampling power-law distributions, *Tectonophysics*, *248*(1-2), 1–20.

Prabhakaran, R., J. L. Urai, G. Bertotti, C. Weismüller, and D. M. Smeulders (2021), Large-scale natural fracture network patterns: Insights from automated mapping in the lilstock (bristol channel) limestone outcrops.

Priest, S., and J. Hudson (1981), Estimation of discontinuity spacing and trace length using scanline surveys, in *International Journal of Rock Mechanics and Mining Sciences & Geomechanics Abstracts*, vol. 18, pp. 183–197, Elsevier.

Priest, S. D., and J. Hudson (1976), Discontinuity spacings in rock, in *International Journal of Rock Mechanics and Mining Sciences & Geomechanics Abstracts*, vol. 13, pp. 135–148, Elsevier.

Prioul, R., and J. Jocker (2009), Fracture characterization at multiple scales using borehole images, sonic logs, and walkaround vertical seismic profile, *AAPG bulletin*, *93*(11), 1503–1516.

Reisenhofer, R. (2014), The complex shearlet transform and applications to image quality assessment, *Master's thesis, Technical University of Berlin*.

Riley, M. S. (2005), Fracture trace length and number distributions from fracture mapping, *Journal of Geophysical Research: Solid Earth*, *110*(B8).

Robinson, P. (1983), Connectivity of fracture systems-a percolation theory approach, *Journal of Physics A: Mathematical and General*, *16*(3), 605.

Ronneberger, O., P. Fischer, and T. Brox (2015), U-net: Convolutional networks for biomedical image segmentation.

Rouleau, A., and J. Gale (1985), Statistical characterization of the fracture system in the stripa granite, sweden, in *International Journal of Rock Mechanics and Mining Sciences & Geomechanics Abstracts*, vol. 22, pp. 353–367, Elsevier.

Sanderson, D. J., and C. W. Nixon (2015), The use of topology in fracture network characterization, *Journal of Structural Geology*, *72*, 55–66.

Sano, O., I. Ito, and M. Terada (1981), Influence of strain rate on dilatancy and strength of oshima granite under uniaxial compression, *Journal of Geophysical Research: Solid Earth*, *86*(B10), 9299–9311.

Santoso, R., X. He, and H. Hoteit (2019), Application of machine-learning to construct simulation models from high-resolution fractured formation, in *Abu Dhabi International Petroleum Exhibition & Conference*, OnePetro.

Segall, P., and D. D. Pollard (1983a), Joint formation in granitic rock of the Sierra Nevada, *Geological Society of America Bulletin*, *94*(5), 563–575.

Segall, P., and D. D. Pollard (1983b), Nucleation and growth of strike slip faults in granite, *Journal of Geophysical Research: Solid Earth*, *88*(B1), 555–568.

Soliva, R., and A. Benedicto (2004), A linkage criterion for segmented normal faults, *Journal of Structural Geology*, *26*(12), 2251–2267.

Song, J.-J., C.-I. Lee, and M. Seto (2001), Stability analysis of rock blocks around a tunnel using a statistical joint modeling technique, *Tunnelling and underground space technology*, *16*(4), 341–351.

Sornette, A., P. Davy, and D. Sornette (1993), Fault growth in brittle-ductile experiments and the mechanics of continental collisions, *Journal of Geophysical Research: Solid Earth*, *98*(B7), 12,111–12,139.

Sornette, D., and A. Sornette (1999), General theory of the modified gutenberg-richter law for large seismic moments, *Bulletin of the Seismological Society of America*, *89*(4), 1121–1130.

Thiele, S. T., L. Grose, A. Samsu, S. Micklethwaite, S. A. Vollgger, and A. R. Cruden (2017), Rapid, semi-automatic fracture and contact mapping for point clouds, images

and geophysical data, *Solid Earth*, *8*(6), 1241–1253.

Tsang, Y. (1984), The effect of tortuosity on fluid flow through a single fracture, *Water Resources Research*, *20*(9), 1209–1215.

Tuckwell, G., L. Lonergan, and R. Jolly (2003), The control of stress history and flaw distribution on the evolution of polygonal fracture networks, *Journal of Structural Geology*, *25*(8), 1241–1250.

Ukar, E., S. E. Laubach, and J. N. Hooker (2019), Outcrops as guides to subsurface natural fractures: Example from the Nikanassin Formation tight-gas sandstone, Grande Cache, Alberta foothills, Canada, *Marine and Petroleum Geology*, *103*, 255–275.

Wang, J., and P. J. Howarth (1990), Use of the hough transform in automated lineament, *IEEE transactions on geoscience and remote sensing*, *28*(4), 561–567.

Watkins, H., C. E. Bond, D. Healy, and R. W. Butler (2015), Appraisal of fracture sampling methods and a new workflow to characterise heterogeneous fracture networks at outcrop, *Journal of Structural Geology*, *72*, 67–82.

Weismüller, C., R. Prabhakaran, M. Passchier, J. L. Urai, G. Bertotti, and K. Reicherter (2020), Mapping the fracture network in the lilstock pavement, bristol channel, uk: manual versus automatic, *Solid Earth*, *11*(5), 1773–1802.

Whitaker, A. E., and T. Engelder (2005), Characterizing stress fields in the upper crust using joint orientation distributions, *Journal of Structural Geology*, *27*(10), 1778–1787.

Wilcock, P. (1996), The NAPSAC fracture network code, in *Developments in geotechnical engineering*, vol. 79, pp. 529–538, Elsevier.

Williams, J. H., and C. D. Johnson (2004), Acoustic and optical borehole-wall imaging for fractured-rock aquifer studies, *Journal of Applied Geophysics*, *55*(1-2), 151–159.

Wyller, F. A. (2019), Spatio-temporal development of a joint network and its properties: a case study from lilstock, uk, Master's thesis, The University of Bergen.

Yeo, I., M. De Freitas, and R. Zimmerman (1998), Effect of shear displacement on the aperture and permeability of a rock fracture, *International Journal of Rock Mechanics and Mining Sciences*, *35*(8), 1051–1070.

Zhu, W., S. Khirevich, and T. Patzek (2018), Percolation properties of stochastic fracture networks in 2d and outcrop fracture maps, in *80th EAGE Conference and Exhibition 2018*, vol. 2018, pp. 1–5, European Association of Geoscientists & Engineers.

Zhu, W., B. Yalcin, S. Khirevich, and T. Patzek (2019), Correlation Analysis of Fracture Intensity Descriptors with Different Dimensionality in a Geomechanics-constrained 3D Fracture Network, in *Petroleum Geostatistics 2019*, vol. 2019, pp. 1–5, European Association of Geoscientists & Engineers.

Zhu, W., S. Khirevich, and T. Patzek (2020), Fracture recognition with u-net and pixel-based automatic fracture detection, in *Fourth Naturally Fractured Reservoir Workshop*, vol. 2020, pp. 1–5, European Association of Geoscientists & Engineers.

Zhu, W., S. Khirevich, and T. W. Patzek (2021a), Impact of fracture geometry and topology on the connectivity and flow properties of stochastic fracture networks, *Water Resources Research*, *57*(7), e2020WR028,652.

Zhu, W., X. He, and T. W. Patzek (2021b), Insights into the coupled effects of fracture geometry and sealing on stimulated reservoir volume in shales, in *3rd International Discrete Fracture Network Engineering Conference*, OnePetro.

Zimmerman, R., S. Kumar, and G. Bodvarsson (1991), Lubrication theory analysis of the permeability of rough-walled fractures, in *International Journal of Rock Mechanics and Mining Sciences & Geomechanics Abstracts*, vol. 28, pp. 325–331, Elsevier.